Xerogel-Derived Ni Electrocatalysts for the Hydrogen Evolution Reaction in Alkaline Media

Mohammed, Doha Mahmoud Sayed
Osmieri, Luigi
Yu, Haoran
Amichi, Lynda
Meyer, Harry M.
Jernigen, Jeremy David
Zelenay, Piotr

To be published in: ACS Applied Energy Materials

DOI to publisher's version: 10.1021/acsaem.5c01048

ACS APPLIED ENERGY MATERIALS

www.acsaem.org Article

Xerogel-Derived Ni Electrocatalysts for the Hydrogen Evolution Reaction in Alkaline Media

Doha M. Sayed,* Luigi Osmieri, Haoran Yu, Lynda Amichi, Harry M. Meyer III, Jeremy D. Jernigen, and Piotr Zelenay*

Cite This: https://doi.org/10.1021/acsaem.5c01048 Read Online

ACCESS | Metrics & More | Article Recommendations | Supporting Information

ABSTRACT: Anion exchange membrane water electrolyzers (AEMWEs) represent a promising technology for hydrogen production. The big advantage of the technology is that it allows for the use of platinum group metal-free (PGM-free) electrocatalysts at both electrodes, including catalysts for the hydrogen evolution reaction (HER) at the cathode. In addition to fulfilling the cost requirement, PGM-free HER catalysts need to meet the activity and durability targets of the AEMWEs. In this work, we developed several carbon-supported, xerogel-derived nickel (Ni) HER electrocatalysts and evaluated the effect of various synthesis conditions, such as the type of carbon support, Ni-to-carbon ratio, and heat-treatment temperature and time, on their performance. Scanning transmission electron microscopy combined with energy-dispersive X-ray spectroscopy (STEM-EDS), X-ray diffraction spectroscopy (XRD), and X-ray photoelectron spectroscopy (XPS) revealed the formation of Ni nanoparticles with an oxygen-rich layer on the outside. Durability of the best-performing catalyst was assessed *via* a constant-current hold at 10 mA cm^{-2} over 100 h. This catalyst was found to be more active and durable than the reference PGM-free material, a commercial Ni catalyst supported on a Vulcan XC-72. The catalyst was also tested in the cathode of a fully PGM-free AEMWE, allowing to reach 1.90 V (1.84 V HFR-free) at 1 A cm^{-2} at 80 °C.

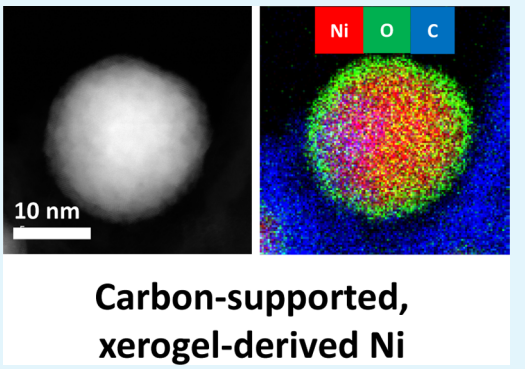

KEYWORDS: *hydrogen evolution reaction, platinum group metal-free electrocatalysts, sol−gel method, nickel electrocatalyst, anion exchange membrane water electrolysis*

INTRODUCTION

Hydrogen is an energy carrier that holds an immense potential for energy storage and conversion.[1,2] It can be produced from a variety of sources, including water electrolysis, by far the most promising method long-term.[3] Proton exchange membrane water electrolyzers (PEMWEs) require platinum group metal (PGM) catalysts, which are the only stable materials in the strongly acidic PEMWE environment. In particular, they rely almost exclusively on iridium for catalyzing the oxygen evolution reaction (OER) at the anode. The high cost of PGM catalysts has hindered widespread commercialization of the PEMWE technology.[4,5] By allowing for the use of PGM-free catalysts, the anion exchange membrane water electrolyzers (AEMWEs) offer an alternative for hydrogen generation at substantially lower cost.[4,6]

In addition to much needed improvements to the performance and durability of anion exchange membranes and ionomers, the ultimate success of AEMWEs requires development of high-performance HER and OER electrocatalysts.[7,8] Nickel-based materials have been widely used to catalyze both OER and HER in alkaline media, exhibiting good activity and durability.[9,10] Inexpensive Raney Ni is a commercially available alloy, often used as an HER catalyst in liquid alkaline water electrolyzers (LAWEs).[11,12] However, HER at this catalyst occurs at a relatively high overpotential of *ca.* 0.30 V.[11] Ni supported on N-doped carbon nanotubes is one of the state-of-the-art PGM-free catalysts for HER/HOR in alkaline media.[13,14] However, it uses an expensive carbon support and relatively elaborate synthesis method, which limit its viability for large-scale application in commercial AEMWEs.[15]

The selection of an Ni-based catalyst synthesis route can remarkably alter the resulting material properties such as surface area, particle size, crystallinity, and ultimately its activity.[16] Therefore, finding novel and easily implementable synthesis methods for Ni-based catalysts is important for further improvements in their performance.[10,17] Ni(II)-based aerogels represent a promising class of materials with relatively high-surface area and small crystallite size (on the order of 5 nm).[18,19] However, their synthesis requires a drying process in

Received: April 8, 2025
Revised: June 17, 2025
Accepted: July 17, 2025

Scheme 1. Synthesis of Xerogel-Derived, Carbon-Supported Ni Electrocatalysts

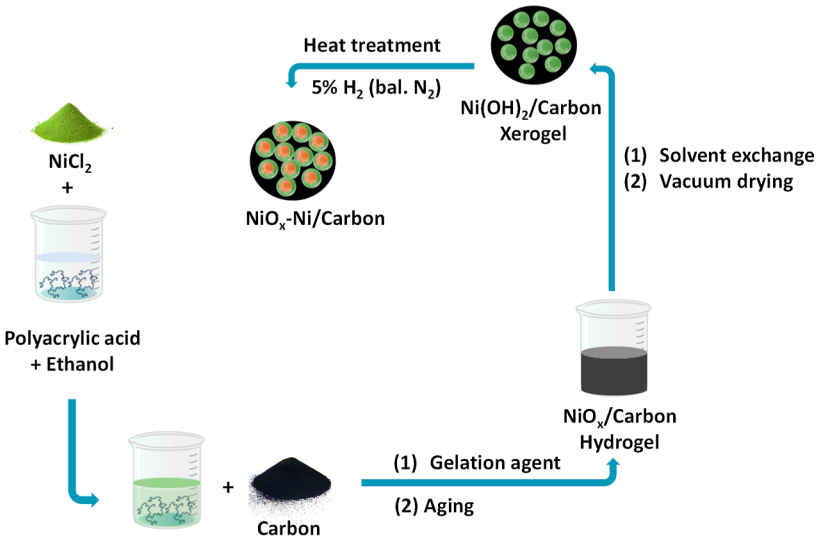

supercritical CO_2 that increases the process cost and complexity.[20,21] Letting the gel dry in air (xerogel synthesis) could help to reduce the complexity and thus the catalyst cost.[22] Introducing carbon into the sol before the gel is formed promises to effectively fill the pores with the gel (Ni precursor). After drying, the thus-obtained xerogel uniformly covers the carbon support, facilitating formation of homogeneously dispersed Ni particles during the heat treatment.[23,24]

While often overlooked in research studies, careful optimization of the synthesis conditions is crucial for performance improvements. Future studies, focusing specifically on rational design of sol−gel-derived electrocatalysts, are expected to result in HER activity improvements. Our findings underscore the importance of optimizing the synthesis conditions of xerogel-derived Ni catalysts to achieve a uniform distribution of Ni nanoparticles and thus enhance the catalytic activity. The type of carbon support and heat-treatment temperature and time are examples of conditions that impact HER performance in a major way. We also found that the formation of a 2−4 nm thick oxygen-rich layer on Ni nanoparticles is essential for attaining high HER activity. We believe that these findings are important for guiding the further development of high-performance HER electrocatalysts for AEMWEs.

EXPERIMENTAL SECTION

Materials. $NiCl_2{\cdot}6H_2O$ (Fisher Scientific), poly(acrylic acid) (PAA, MW = 450,000, Sigma-Aldrich), ethanol (200 proof, Sigma-Aldrich), Vulcan XC-72 (VC) (Cabot), Ketjenblack (KB) EC-300J (Nouryon), Black Pearls (BP2000) (Cabot), propylene oxide (PO, Sigma-Aldrich), KOH pellets (Sigma-Aldrich, ACS reagent grade purity), 40% Ni catalyst supported on Vulcan XC-72 (Fuel Cell Store), D521 Nafion dispersion (5 wt %, equivalent weight 1100 g eq^{-1}, Ion Power), and PiperION-A5-HCO3EtOH dispersion (5 wt %, equivalent weight 425.5 g eq^{-1}, Versogen) were used.

Catalyst Synthesis. Xerogel-derived, carbon-supported Ni HER catalysts were prepared by using a sol−gel method (Scheme 1). PAA (25 mg), a nucleation agent,[19] was first dissolved in 17.5 mL of ethanol, followed by addition (1.80 g) of a Ni precursor ($NiCl_2{\cdot}6H_2O$) to form the sol. Once complete dissolution was achieved, carbon was dispersed in the solution, and 2 mL of a gelation agent (propylene oxide, PO) was slowly added at a rate of *ca.* 1 mL min^{-1} to form a hydrogel, which was then aged by storing in a closed vial for 2 days at room temperature and then washed with ethanol to remove remaining PO. Ethanol was replaced four times over 48 h to ensure thorough gel washing. To form the xerogel, the solvent was first evaporated in a fume hood for few hours at room temperature, then the vial was placed in a vacuum oven at 60 °C overnight. The xerogel (*ca.* 0.15 g) was heat-treated under a reducing atmosphere (5% H_2 in N_2) in a tube furnace to yield the catalyst (Ni-XG/C). A carbon-free catalyst (Ni-XG) was obtained using the same procedure but without carbon addition. We investigated several synthesis conditions such as (i) ex-situ carbon addition (xerogel mechanically mixed with the carbon support before the heat treatment); (ii) type of carbon support; (iii) aerogel *vs* xerogel synthesis approaches; (iv) Ni-to-carbon ratio (1:1, 2:1, and 3:1); (v) heat-treatment temperatures (300, 400, and 500 °C); and (vi) heat-treatment time (1, 2, and 3 h). These conditions for all catalysts in this study are summarized in Table S1.

For the synthesis of the aerogel-derived catalyst, the gel was dried in supercritical CO_2, transferred into a stainless-steel sample-holder equipped with a fine (2 μm) metal grid, and then inserted into a chamber of an automated supercritical CO_2 dryer (Autosamdri-931, Tousimis, USA). The chamber was filled with ethanol before the supercritical drying process was started. Drying consisted of 5 cycles of purging with liquid CO_2, each followed by 3 h dwell time, with a final step of holding at supercritical conditions (38 °C and 82 bar) for 2 h.

Physical and Chemical Characterization. *X-ray Diffraction (XRD).* XRD patterns were collected to determine the crystallographic structure of the catalysts. Measurements were performed on a Siemens D5000 diffractometer using a Cu K_α radiation source and a graphite monochromator. Diffraction patterns were recorded in the 2θ range between 20° and 90° with a 0.1° step. Jade9 software was used to determine crystallographic phases associated with the XRD peaks.

X-ray Photoelectron Spectroscopy (XPS). XPS characterization was carried out using a Thermo Scientific (Waltham, MA, USA) Model K-Alpha instrument, utilizing monochromated, microfocused, Al K_α X-rays (1486.6 eV) with a variable spot size (30−400 μm). A 400 μm X-ray spot was used for the maximum signal and to obtain an average surface composition over the largest possible area. The instrument had a hemispherical electron energy analyzer equipped with a 128-channel detector system. Base pressure in the analysis chamber was typically 2×10^{-9} mbar or lower. The powders were prepared for analysis by dispersing materials onto double-sided tape on clean glass slides. Sufficient material was used to prevent any interference signals from the tape. For analyzing the impact of durability on the surface composition, two electrodes were prepared using carbon paper as a substrate where the ink (5 times the volume used in the RDE experiments) was cast on 1 cm^2 electrode area. The

https://doi.org/10.1021/acsaem.5c01048
ACS Appl. Energy Mater. XXXX, XXX, XXX−XXX

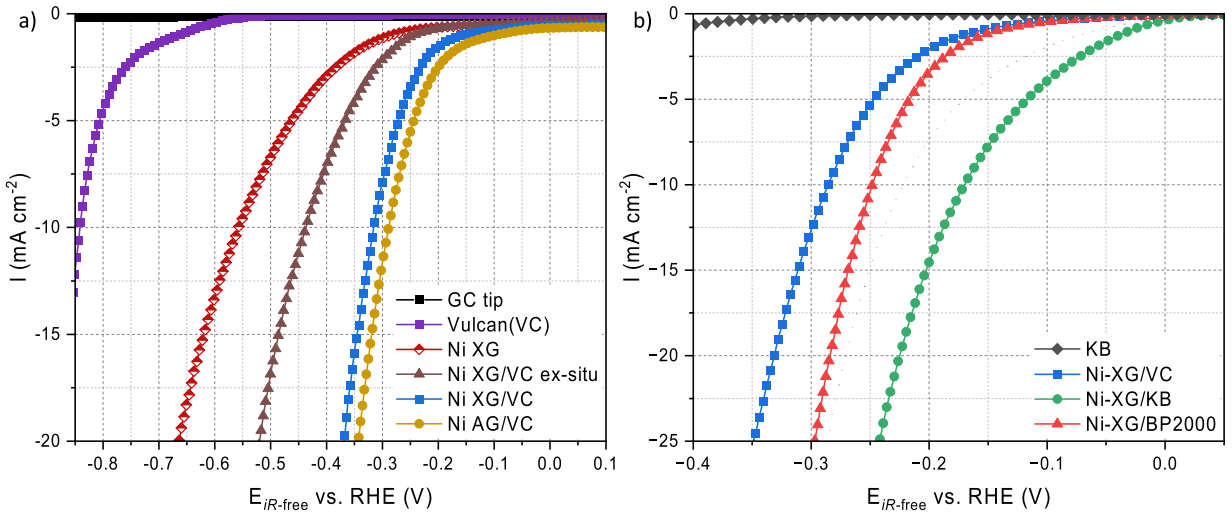

Figure 1. *iR*-corrected polarization curves measured in the RDE cell with (a) various HER catalysts (polarization plots for Vulcan and GC tip alone given to demonstrate negligible activity of the carbons) and (b) Ni-XG supported on different carbons (compared with KB alone). Catalysts heat-treated 500 °C for 2 h; Ni-to-C ratio 3:1; 0.1 M KOH electrolyte; RDE at 2500 rpm.

first electrode was tested only for the initial HER activity. The second electrode was also subjected to the HER durability test *via* a constant-current hold at 10 mA cm^{-2} for 20 h. The electrodes were attached directly to the XPS sample holder by using metal clips. After the sample was transferred into the analysis chamber, a survey spectrum (step size 1 eV, pass energy 200 eV) was acquired to determine all elements present. Next, high-resolution core level spectra (step size 0.1 eV, pass energy 50 eV) were acquired for a detailed chemical state analysis. C KLL (Auger) spectra were recorded using a step size of 2 eV and a pass energy of 100 eV. All spectra were acquired with the charge neutralization flood gun (combination of low energy electrons and argon ions) turned on to maintain stable analysis condition. A typical pressure in the analysis chamber with the flood gun operating was 2×10^{-7} mbar. Data were collected and processed using the Thermo Scientific Avantage XPS software package (v.5.96).

Electron Microscopy. Scanning electron microscopy (SEM) images were acquired using a Quattro S microscope (ThermoScientific) operated at 20 kV. Catalyst morphology and composition were determined by aberration-corrected scanning transmission electron microscopy (STEM) using a JEOL NEOARM equipped with dual 100 mm^2 solid-state detectors for energy-dispersive X-ray spectroscopy (EDS). High-angle annular dark-field (HAADF) images were recorded at 200 kV by using DigitalMicrograph software (Gatan, Inc.). Atomic-resolution STEM-EDS maps were acquired and processed in JEOL analysis station software using the standardless Cliff-Lorimer routine. For investigating the impact of durability, the previously mentioned two carbon paper electrodes (XPS section) were further analyzed *via* STEM-EDS.

BET Surface Area and Pore Size Distribution. The surface area and pore-size distribution of some of the catalysts were measured with a Quantachrome Autosorb-iQ instrument at 77 K using liquid N_2. Before the analysis, the samples were placed in the glass sample tube used for the analysis and degassed under vacuum for 3 h at 180 °C. The surface area was calculated using the Brunauer–Emmett–Teller (BET) method within the relative pressure range of 0.05 and 0.3 on the adsorption isotherm branch. The pore volume and pore-size distribution were obtained using the Barrett–Joyner–Halenda (BJH) method included in instrument software.

Electrochemical Testing. *Three-Electrode Cell Testing.* A rotating disk electrode (RDE) setup (Pine Research, USA) and a BioLogic SP-300 potentiostat were used to evaluate the HER activity of catalysts. The working electrode was prepared by drop-casting the catalyst ink onto a glassy carbon (GC) tip. The ink was prepared similarly to a procedure used previously.[18,25] Briefly, 7 mg of the catalyst powder was dispersed into a mixture of deionized water and 2-propanol at a volume ratio of 2:1. Neutralized D521 Nafion ionomer suspension was added to the mixture as a binder. The ink was then sonicated for 30 min to form a homogeneous dispersion, and an aliquot was pipetted onto a GC tip to obtain the desired catalyst loading. Metal loading was adjusted to be *ca.* 0.5 mg cm^{-2}, and the ionomer-to-catalyst ratio was kept at 0.6. A reversible hydrogen electrode (RHE) and a graphite rod were used as the reference and counter electrodes, respectively. The electrolyte solution was 0.1 M KOH (or 1.0 M KOH in durability experiments) saturated with Ar gas. The electrochemical tests were performed using a PTFE cell to avoid any possible corrosion of glass components in contact with the alkaline electrolyte. The HER test protocol consisted of 10 cyclic voltammograms (CVs) between 0.0 and 1.0 V *vs* RHE at a scan rate of 50 mV s^{-1}, followed by additional 3 cycles at 10 mV s^{-1} in the same potential range. Finally, 3 more CV cycles at 50 mV s^{-1}, followed by 3 CV cycles at 10 mV s^{-1}, were measured between 0.4 and −0.50 V *vs* RHE.

The HER activity was evaluated by staircase voltammetry (SV) in the potential range between 0.1 and −0.5 V *vs* RHE using 10 mV potential steps and 10 s hold time at each potential in both forward and backward scan directions. The rotation speed was set to a high value of 2500 rpm to minimize the H_2 bubble growth and to ease their removal from the catalyst layer surface. The high-frequency resistance (HFR) was measured by electrochemical impedance spectroscopy (EIS). The EIS measurements were performed in both the potentiostatic mode at the open-circuit potential and the galvanostatic mode at 10 mA cm^{-2} in the frequency range from 1 Hz to 100 kHz. The intercept with the real axis of the EIS Nyquist plot was used to correct the polarization curves for the ohmic (*iR*) drop. Both EIS measurement modes yielded the same HFR values. *iR*-correction of the polarization curves was performed on the raw experimental data.

Catalyst durability was assessed through a protocol that involved HER testing to evaluate catalytic activity at the beginning of the test (BOT), followed by constant-current hold at a current density of 10 mA cm^{-2} for 100 h, and HER testing to evaluate catalytic activity at the end of the test (EOT). The catalyst degradation rate is expressed in terms of a per-hour potential loss at a current density of 10 mA cm^{-2} (mV h^{-1}), based on polarization curves recorded at BOT and EOT.

MEA Preparation. Membrane electrode assemblies (MEAs) for AEMWE testing were prepared as described before.[18] The anode catalyst, labeled PTL-supported NiFe/Ni-foam, was an ionomer-free Ni–Fe hydroxide on the surface of a commercial Ni foam, and it was synthesized *via* a modified Fe-catalyzed Ni foam approach, reported elsewhere,[26] with some modifications to the precursors and reaction time. The carbon-supported xerogel-derived Ni cathode catalyst was sprayed onto a piece of carbon paper (MGL370, AvCarb) using an

https://doi.org/10.1021/acsaem.5c01048
ACS Appl. Energy Mater. XXXX, XXX, XXX−XXX

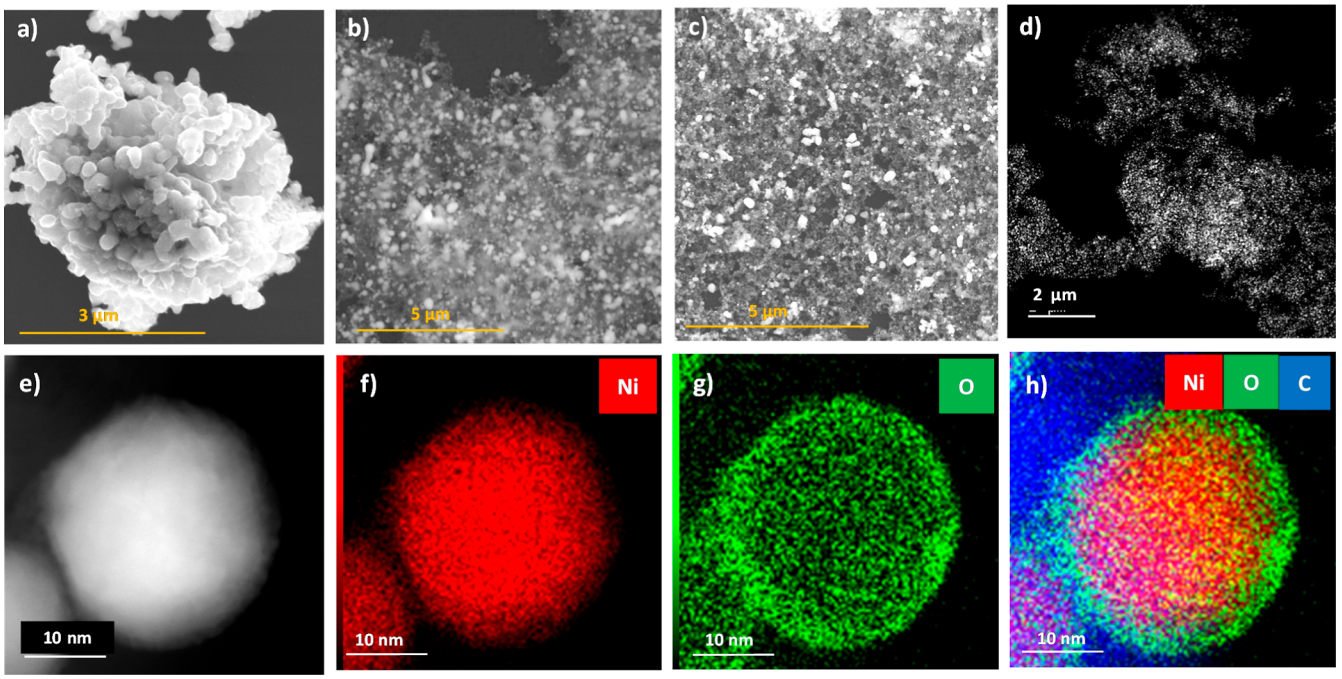

Figure 2. SEM images of (a) Ni-XG (carbon-free), (b) Ni-AG/VC, and (c) Ni-XG/VC. (d) Low-magnification HAADF image of Ni-XG/KB, (e) high-magnification HAADF-STEM image of the Ni-XG/KB catalyst, and (f–h) corresponding STEM-EDS maps of Ni, O, and Ni + O + C). Catalyst heat-treated at 500 °C for 2 h; Ni-to-C ratio 3:1.

automated ultrasonic spray coating system (Sono-Tek ExactaCoat). The catalyst powder was mixed with DI water, IPA, and a commercial anion exchange ionomer (PiperION-A5-HCO3EtOH,Versogen) to prepare the catalyst ink for electrode spraying. For comparison, a PGM benchmark cathode was prepared using a commercial PtRu/C catalyst (Pt 20%, Ru 10% on carbon black, HiSPEC 10000, Alfa Aesar). The metal loading of the carbon-supported xerogel-derived Ni catalyst was adjusted to be *ca.* 1.25 mg cm^{-2}, and the ionomer-to-catalyst ratio was kept as 0.45. As for the commercial PtRu/C catalyst, the total metal loading was *ca.* 0.75 mg cm^{-2} and the ionomer-to-catalyst ratio was kept as 0.77. Before testing, catalyst-coated substrates (CCSs) were stored in 1 M NaOH solution overnight to convert ionomer from the original HCO_3^- form to the OH^- form.[18] Commercial AEMs (PiperION-A40-HCO3, Versogen) were also treated with 1 M NaOH for the same purpose before their assembly in the cell hardware for electrolyzer testing. The anode and the cathode were placed on opposite sides of the membrane and held together with two fiber-reinforced PTFE gaskets (250 μm thickness) inside the cell hardware. No hot pressing was used.

AEMWE Testing. AEMWE testing was carried out at either 70 or 80 °C with 1 M KOH flowing only through the anode compartment at a flow rate of 10 mL min^{-1}. Polarization curves were recorded using a BioLogic VMP3 potentiostat operating with a VMP3B-20 booster (20 A maximum current) in the constant-current mode between 0.1 and 2.0 A cm^{-2} and 3 min holds at each current density. The voltage values were collected every 0.1 A cm^{-2} over the last 30 s of each step and then averaged. Electrochemical impedance spectra were logged in the constant-current mode between 0.1 and 1 A cm^{-2} to determine the HFR value for the *i*R-correction of polarization curves as described before. Durability experiments were carried out at 80 °C *via* a constant-current hold at 1 A cm^2.

RESULTS AND DISCUSSION

Effect of Carbon Substrates. We explored the effect of *ex situ vs in situ* addition of carbon (Vulcan XC-72, VC) to a carbon-free xerogel-derived Ni catalyst (Ni-XG). The current density of 10 mA cm^{-2} was reached with Ni-XG at *ca.* −0.55 V (*i*R-corrected), Figure 1a, which decreased by *ca.* 100 mV following *ex situ* carbon addition (the "Ni-XG/VC *ex situ*" plot in Figure 1a), and by *ca.* 140 mV more after the *in situ* carbon addition ("Ni-XG/VC" plot in Figure 1a). An SEM image of the Ni-XG catalyst synthesized in the absence of carbon (Figure 2a) points to the agglomeration of Ni, which reduces the surface area available for the reaction. This surface area loss can explain inferior HER performance of Ni-XG.

According to previous reports, the drying method (vacuum oven *vs* supercritical CO_2 drying) can impact the structure and morphology of the resulting Ni oxide/hydroxide.[27−29] For example, Jiang et al. measured higher surface and smaller particle size with Ni/Al_2O_3 aerogel compared to the xerogel.[29] Figure 1a also includes comparison of the xerogel-derived Ni catalyst and the aerogel-derived one (Ni-AG/VC) after an *in situ* addition of the carbon. The performance difference between the two catalysts was no more than 10 mV at 10 mA cm^{-2}. Figure 2b,c shows that both the aerogel- and xerogel-derived Ni catalysts have a similar morphology. The VC addition allowed for achieving a similar dispersion of the two catalysts after the heat treatment, preventing the particle agglomeration observed in Figure 2a. Given these results, we selected the xerogel synthesis approach with *in situ* carbon addition (Scheme 1) for further investigation as it does not require the more complex drying step in supercritical CO_2.

Next, we investigated the effect of different carbon supports on the performance of the xerogel-derived catalyst. Figure 1b summarizes the performance of xerogel-derived Ni catalysts synthesized under the same conditions (Ni-to-C ratio of 3:1, heat treatment at 500 °C for 2 h) but supported on three different commercial carbons: Ketjenblack (KB), Vulcan (VC), and Black Pearls 2000 (BP200). Ni-XG/KB showed the best HER performance with the reference current density of 10 mA cm^{-2} reached at −0.17 V (*i*R-corrected). The performance was lower with Ni-XG catalyst supported on Black Pearls (BP2000) and Vulcan (VC), with 10 mA cm^{-2} reached at

https://doi.org/10.1021/acsaem.5c01048
ACS Appl. Energy Mater. XXXX, XXX, XXX−XXX

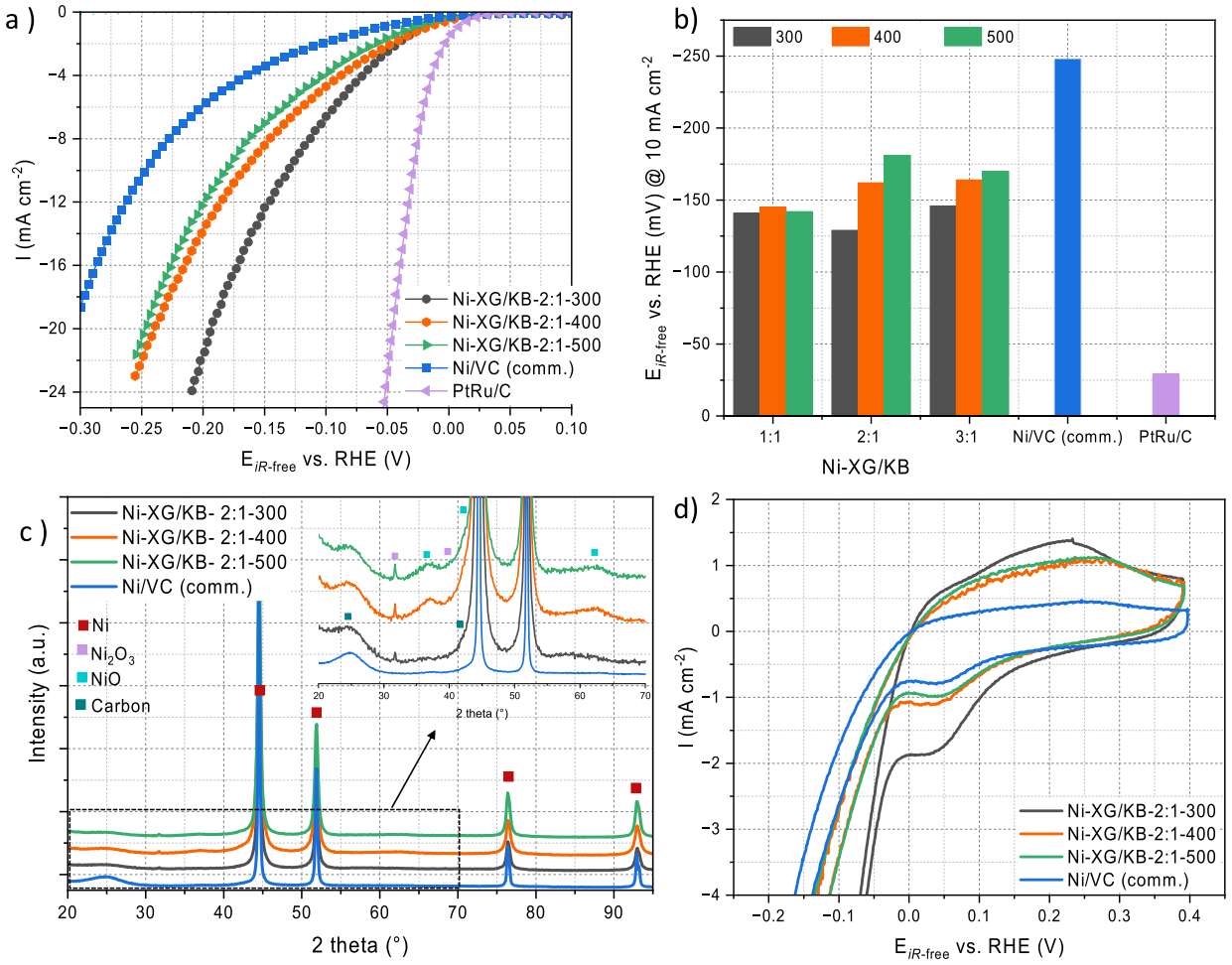

Figure 3. (a) *iR*-corrected polarization curves measured in the RDE cell with Ni-XG/KB-2:1 catalysts heat-treated at various temperatures for 2 h; polarization curves for commercial Ni/VC and PtRu/C catalysts included for comparison. (b) *iR*-corrected potentials *vs* RHE at a current density of 10 mA cm^{-2} for different HER catalysts. (c) XRD images and (d) cyclic voltammograms recorded with Ni-XG/KB-2:1 catalysts heat-treated at various temperatures for 2 h and commercial Ni/VC catalysts. 0.1 M KOH electrolyte; RDE at 2500 rpm; scan rate in (d) 10 mV s^{-1}.

−0.25 V and −0.29 V, respectively. These results demonstrate that the carbon support can play an important role in increasing HER activity of Ni catalysts, possibly by assuring homogeneous dispersion and enhancing the surface area of the catalyst. This can be linked in turn to morphological properties of the supports, such as their specific surface area and pore-size distribution.[30] See the Supporting Information, Figure S1 and Table S2 for the surface area, pore-size distribution results, and more details. A low-magnification HAADF-STEM image of Ni-XG supported on KB shown in Figure 2d attests to uniform distribution of small Ni nanoparticles, which likely results in a surface-area enhancement and increased activity relative to Ni-XG and Ni-XG/VC catalysts. A high-magnification HAADF-STEM image of Ni-XG/KB in Figure 2e reveals a spherical morphology of the nanoparticles with an average diameter of *ca.* 20 nm. STEM-EDS maps in Figure 2f–h further points to a metallic Ni core and oxygen-rich, 2–4 nm thick layer on the outside, likely the result of the catalyst exposure to atmospheric air after the heat treatment.[31]

Effect of Heat-Treatment Temperature and Ni-to-C Ratio. The as-synthesized xerogel, composed mostly of $3Ni(OH)_2{\cdot}2H_2O$ (PDF#00-022-0444, see XRD image in Figure S2a), was found to be HER inactive (Figure S2b). It was the heat treatment that proved to be crucial for imparting HER activity. Heat-treating the xerogel above 500 °C (e.g., 750 °C) and below 300 °C (e.g., 250 °C) resulted in a significant increase in the HER overpotential (Supporting Information, Figures S3a,b for more details). Thus, we explored the effect of heat treatment over a narrower range of temperature, that is, 300, 400, and 500 °C on Ni-XG/KB catalysts with three different Ni-to-C ratios (1:1, 2:1, and 3:1) to assess whether the impact of temperature on HER performance remains consistent across these ratios. The RDE polarization curves for the best-performing catalyst, Ni-XG/KB-2:1, obtained at the three heat-treatment temperatures are shown in Figure 3a, while the results for catalysts with two other Ni-to-C ratios, 1:1 and 3:1, are summarized in Figure S4. Figure 3a also shows polarization plots recorded with a commercial PtRu/C, benchmark HER catalyst for alkaline media,[32,33] and with commercial 40 wt % Ni catalyst supported on Vulcan XC-72.

Figure 3b offers an activity comparison for all studied catalysts at a reference current density of 10 mA cm^{-2}. All xerogel-derived Ni-XG catalysts show superior HER activity, by between 50 and 100 mV, to that of the commercial Ni/VC catalyst, with Ni-XG/KB-2:1 heat-treated at 300 °C delivering 10 mA cm^{-2} at the lowest overpotential of −0.13 V. However, even the most active of Ni-XG/KB catalysts trails the benchmark PtRu/C catalyst by *ca.* 100 mV. This performance

https://doi.org/10.1021/acsaem.5c01048
ACS Appl. Energy Mater. XXXX, XXX, XXX−XXX

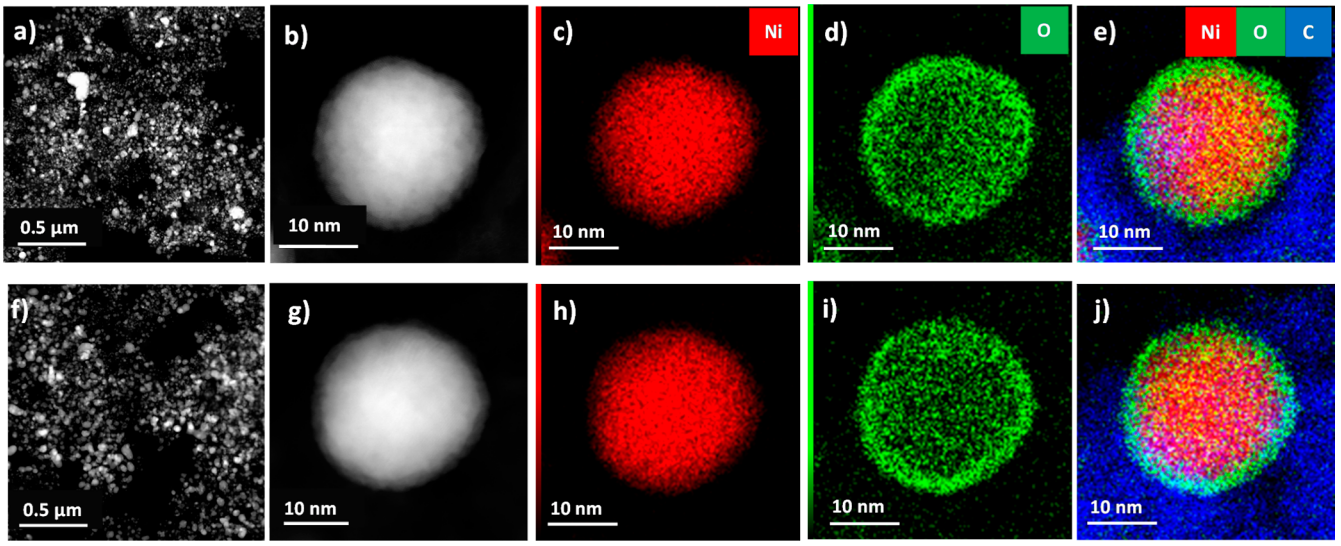

Figure 4. (a,b) HAADF-STEM and (c–e) Ni, O, and Ni + O + C STEM-EDS maps for Ni-XG/KB-2:1–300 heat-treated for 2 h. (f,g) HAADF-STEM and (h–j) Ni, O, and Ni + O + C STEM-EDS maps for Ni-XG/KB-2:1–500 heat-treated for 2 h.

gap needs to be reduced before the cost benefit of Ni catalysts balances out the activity advantage of the PtRu alloy.[12,34] Ideally, the HER overpotential should be lowered to *ca.* 50 mV at 10 mA/cm^2.[34]

The effect of the heat-treatment temperature on the HER activity was more obvious, especially for catalysts with Ni-to-C ratios of 2:1 and 3:1 (Figures 3a and S4). With Ni-to-C ratio 2:1, a decrease in the HER performance was observed when the heat-treatment temperature increased from 300 to 500 °C. XRD images of these three catalysts as well as that of the commercial Ni/VC catalyst are shown in Figure 3c. All catalysts contain Ni nanocrystals, the presence of which gives rise to XRD peaks at 2θ values of 44.4, 51.8, 76.3, and 92.9° (PDF#01-071-3740) in Figure 3c. They correspond to diffractions from the (111), (200), (220), and (311) planes in Ni. The peak at 23° is assigned to the main (002) plane of turbostratic carbon.[35] More information on Ni-XG/KB-2:1 can be gained from the inset in Figure 3c that focuses on the 2θ range from 20° to 70°. Characteristic peaks for two Ni-oxide phases are observed in the xerogel-derived samples (not present in commercial Ni/VC sample). Peaks at 2θ values of 37.2, 43.3, and 62.8° are assigned to NiO (PDF#00-044-1159), and the peak at 31.9° is assigned to the (002) plane of Ni_2O_3 (PDF#00-014-0481). According to XRD results for Ni-XG/KB-2:1 in Figure 3c, there is a negligible increase in metallic nickel peak intensities and average crystallite sizes calculated from XRD patterns (*ca.* 0.6 nm) in these catalysts with increasing temperature. The average crystallite size of the commercial Ni/VC is *ca.* 27 nm, which is *ca.* 1.6 times larger than that in Ni-XG/KB-2:1 catalysts, see Table S3. This observation likely explains the lower performance of the commercial Ni/VC compared to our catalysts.

To better understand the temperature effect, we conducted voltammetric characterization of the three Ni-XG/KB-2:1 catalysts and the commercial Ni/VC catalyst. The CV cycles of fully broken-in catalysts in the potential range from 0.4 to −0.5 V are shown in Figure 3d (the figure displays only the zoomed-in portion to focus on differences in the Ni redox peaks). They reveal very similar redox behavior attributed to the Ni metal oxidation/Ni hydroxide reduction[36,37]

$$Ni + 2H_2O \rightleftarrows Ni(OH)_2 + 2H^+ + 2e^- \quad (1)$$

The peak heights are different for the different catalysts, despite the same catalyst loading used. There is a decrease in the height of Ni redox peaks with an increase in the heat-treatment temperature from 300 to 500 °C, indicating a possible reduction in the active surface area of Ni.[38,39] The lowest peak height was recorded with the commercial Ni/VC catalyst, which correlates well with less active surface area and different surface composition of this catalyst compared with the Ni-XG/KB-2:1 catalysts (confirmed by microscopy and XPS results below). The STEM-EDS images of Ni-XG/KB-2:1–300 (Figure 4a–e) and Ni-XG/KB-2:1–500 (Figure 4f–j) do not show significant growth in the particle size with an increase of heat-treatment temperatures. This is also evident in the low-magnification images in Figure S5. HAADF-STEM images of the commercial catalyst are shown in Figure S6, which reveal poor dispersion of Ni particles on the VC support that should reduce active surface available for HER. High-magnification STEM–EDX images of an individual particle in the commercial Ni/VC (Figure S7) are very similar to those of Ni-XG/KB (Figure 4), although the Ni particle size is larger in the commercial catalyst. This attests to the effectiveness of the xerogel synthesis approach that results in uniform distribution of small Ni particles on the carbon support.

The oxygen-rich outer layer in the nanoparticles is more than 2 nm thick and is likely to play an important role in HER electrocatalysis. Arguably, the main challenge in alkaline water electrolysis is the need for an energy input to cleave the H–OH bond to produce an H atom. It has been suggested that the presence of oxygen-containing species on the catalyst surface should favor HER since water is the proton source in alkaline media (slow kinetics compared to acid where protons are present).[40] In support of this concept, $Ni(OH)_2$ has been found to be an effective cocatalyst for various HER catalysts, e.g., Pt, Ru, and Ni.[37,41,42] Subbaraman et al. found that $Ni(OH)_2$ clusters on the platinum surface accelerate dissociative adsorption of water and enhance adsorption rate of hydrogen intermediates on the nearby Pt metal site.[41] For the Ni-XG/KB-2:1 catalysts, the change in activity with the heat-treatment temperature can be attributed to a change in

https://doi.org/10.1021/acsaem.5c01048
ACS Appl. Energy Mater. XXXX, XXX, XXX–XXX

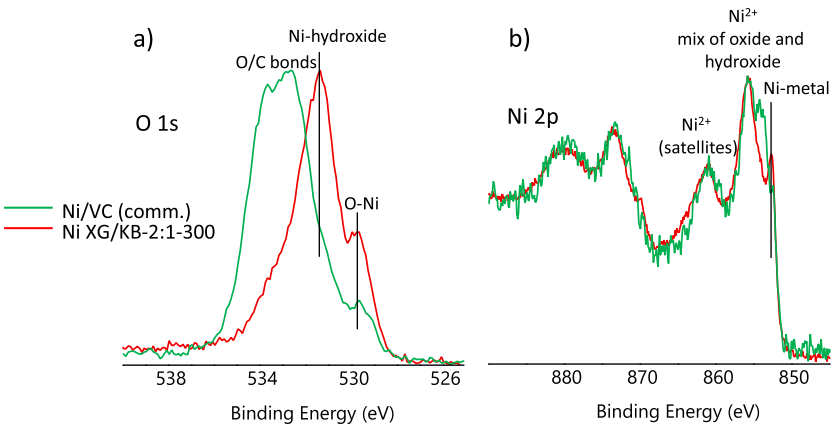

Figure 5. High-resolution XPS data of Ni-XG/KB-2:1−300 heat-treated for 2 h and commercial Ni/VC catalyst: (a) O 1s; (b) Ni 2p. Data in Figure 3b above point to relatively small effect of the Ni-to-C ratio on HER activity of Ni-XG/KB catalysts. In the specific case of the most active catalysts heat-treated at 300 °C, the activity differences for samples with different Ni-to-C ratios are especially small.

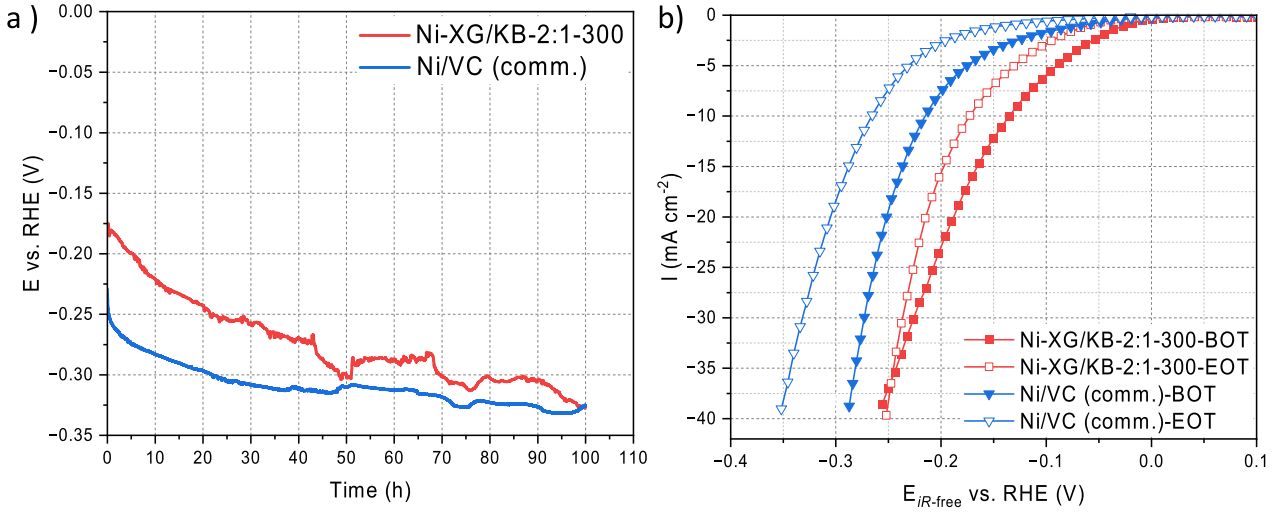

Figure 6. (a) Durability curves at constant-current hold of 10 mA cm^{-2} in the RDE cell recorded with Ni-XG/KB-2:1−300 catalyst heat-treated for 2 h and commercial Ni/VC catalyst. (b) *iR*-corrected polarization curves for the two catalysts recorded at the beginning and end test. 1 M KOH electrolyte; RDE at 2500 rpm.

the oxygen content on the surface of the nanoparticles. EDS shows O-to-Ni ratio of 0.41 after the heat treatment at 300 °C that decreases to 0.24 following heat treatment at 500 °C. Elemental content values obtained from STEM-EDS images in Figure S5 are given in Table S4. The decrease in the oxygen content in the sample heat-treated at higher temperature is likely the result of harsher reducing conditions.

To gain more information on the surface/near-surface catalyst composition, we conducted XPS characterization of the best-performing Ni-XG/KB-2:1−300 catalyst heat-treated for 2 h and of the commercial Ni/VC catalyst. According to the survey spectra in Figure S8 and near-surface elemental composition Table S5, the total C content in commercial Ni/VC catalyst is higher than that in Ni-XG/KB-2:1−300 (*ca.* 90 at. % *vs ca.* 82 at. %), while the Ni content is higher in Ni-XG/KB-2:1−300 (*ca.* 6 at. % *vs ca.* 1 at. %). Both catalysts contain *ca.* 10 at. % O (Ni-XG/KB-2:1−300 also contained small amounts of Cl and Na *ca.* 1 at. % that are likely residuals from the precursors used in the xerogel synthesis process). C 1s, O 1s, and Ni 2p core level spectra of the two samples are shown in Figures S9 and 5. The C 1s spectrum for the Ni-XG/KB-2:1−300 sample is due to C−C (sp2), with π to π^* satellite structure at a binding energy of 290−294 eV, Figure S9. As for the C 1s spectrum of the commercial Ni/VC, Figure S9, the peak is also due to C−O and O=C−O species.[35] The O 1s spectra for both samples show peak at *ca.* 530 eV assigned to O−Ni bond, i.e., an Ni oxide, and another peak at *ca.* 531.5 eV assigned to Ni-hydroxide, Figure 5a.[18] The O 1s spectrum for the Ni/VC sample shows prominent peaks related to the O−C bonds, consistent with the C 1s data, Figure S9. The Ni 2p spectrum of Ni-XG/KB-2:1−300 shows a prominent Ni-metal peak along with Ni-hydroxide and Ni-oxide peaks at higher BE values, Figure 5b. On the other hand, the commercial Ni/VC catalyst shows very little, if any, metallic content at/near the surface and complex surface oxide/hydroxide structure, Figure 5b.[43] The XPS results confirm the partial surface oxidation of the xerogel-derived catalyst. The coexistence of metallic Ni with oxides and hydroxides in Ni-XG/KB-2:1−300 could explain higher HER activity of this catalyst compared to the commercial Ni/VC material, which does not show any presence of metallic nickel on the surface. The latter hypothesis agrees with Gong et al., who measured better HER performance with a catalyst containing both nickel oxide and metallic nickel phases, compared to materials based on

https://doi.org/10.1021/acsaem.5c01048
ACS Appl. Energy Mater. XXXX, XXX, XXX−XXX

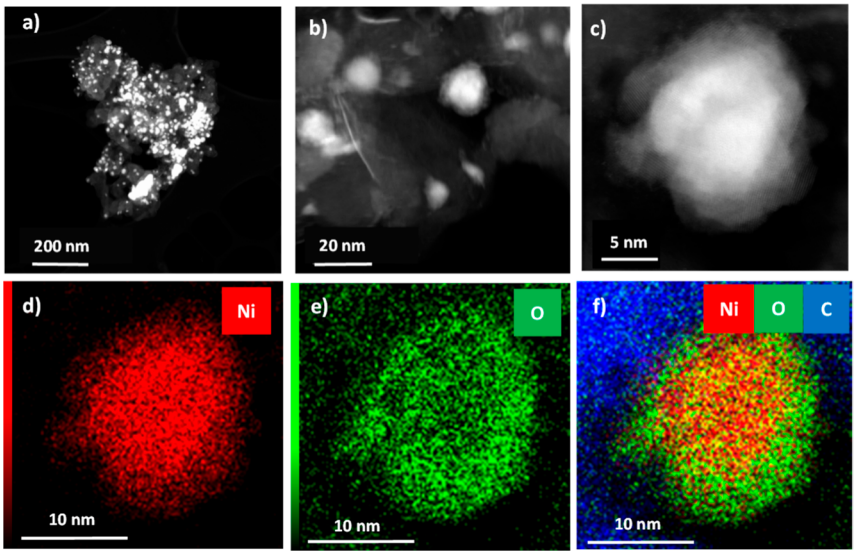

Figure 7. (a–c) HAADF-STEM images at various magnifications and (d–f) Ni, O, and Ni + O + C STEM-EDS maps of Ni-XG/KB-2:1–300 catalyst, heat-treated for 2 h, after the durability testing. See HAADF-STEM and STEM-EDS images at the BOT in Figure 4a–e.

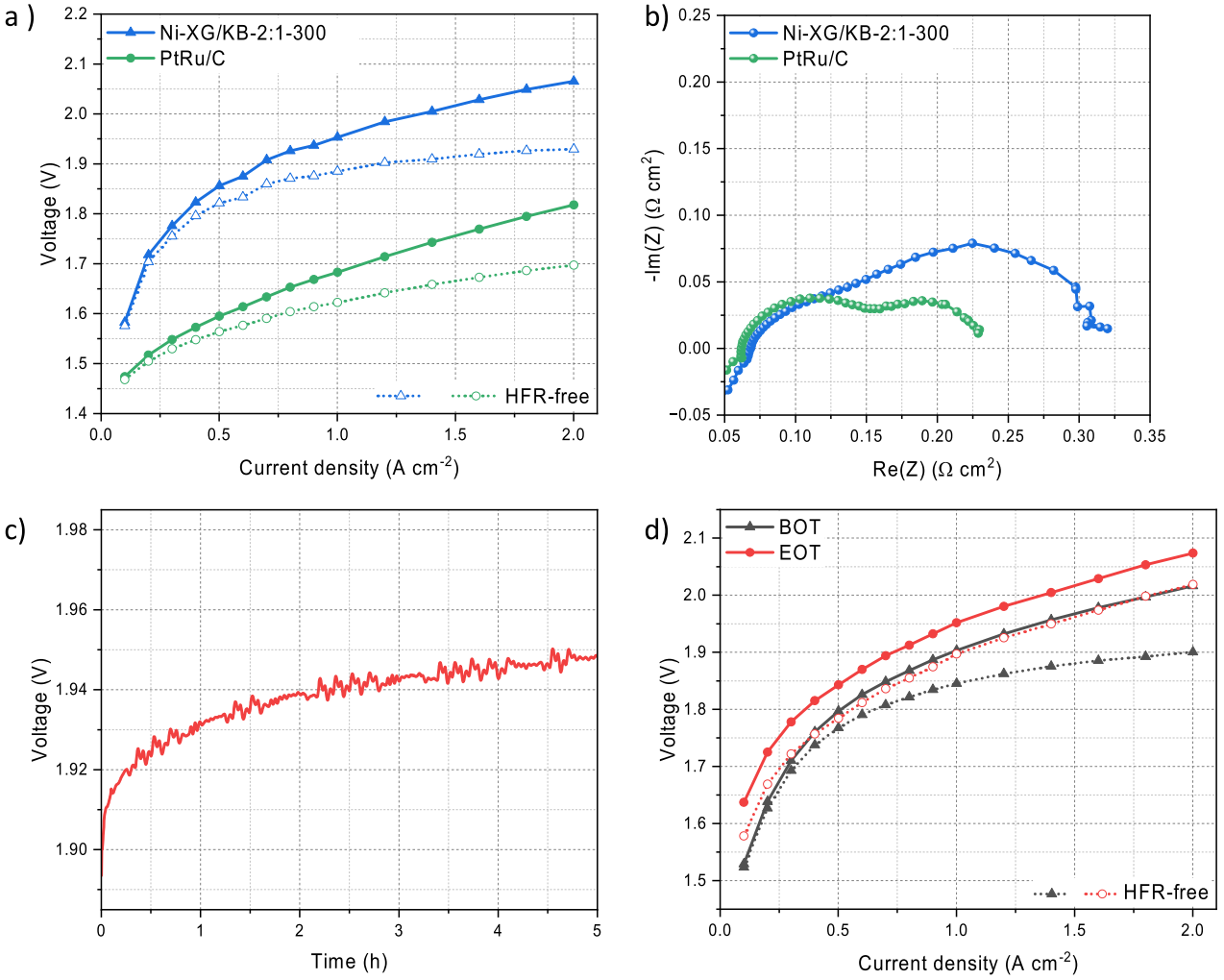

Figure 8. (a) AEMWE polarization curves recorded with Ni-XG/KB-2:1–300 catalyst heat-treated for 2 h and PtRu/C cathode catalyst at 70 °C and (b) corresponding Nyquist plots obtained with both MEAs. (c) Durability curve at constant-current hold of 1 A cm^{-2} and (d) AEMWE polarization curves recorded with Ni-XG/KB-2:1–300 catalyst in the cathode at the beginning and end test at 80 °C. 1 M KOH fed to the anode (PTL-supported NiFe/Ni-foam).

https://doi.org/10.1021/acsaem.5c01048
ACS Appl. Energy Mater. XXXX, XXX, XXX–XXX

pure metallic Ni or NiO.[43] This was explained by preferential binding of OH^- generated from water dissociation to NiO (strong electrostatic affinity to positively charged Ni^{2+} species), with a nearby Ni site facilitating H adsorption and thus the HER.[43] In this context, it is worth noting that Ni oxides/hydroxides are known to be poor HER catalysts due to an unfavorable adsorption energy of the hydrogen atom at their surfaces.[44−46]

We also studied the impact of heat-treatment time for the best-performing Ni-XG/KB-2:1−300 for time durations of 1, 2, and 3 h (see the Supporting Information, Figure S10a,b for more details). No enhancement was observed when the heat-treatment time extended or reduced from 2 h. Table S6 lists the HER performance of our best-performing catalyst and other Ni and Ni-based catalysts reported in the literature.

Durability Measurements. The durability of the Ni-XG/KB-2:1−300 catalyst heat-treated for 2 h and of the commercial Ni/VC catalyst was assessed at a constant current density of 10 mA cm^{-2} over 100 h (Figure 6a). The potential loss incurred at that current density by Ni-XG/KB-2:1−300, calculated from the polarization plots in Figure 6b, was from *ca.* −0.13 V at the beginning of test (BOT) to *ca.* −0.17 V at the end of test (EOT), which corresponds to an average performance degradation rate of *ca.* 0.4 mV h^{-1}. By comparison, the commercial Ni/VC catalyst delivered 10 mA cm^{-2} at BOT at a significantly lower potential of *ca.* −0.21 V, which decreased to *ca.* 0.26 V at EOT for an average performance loss of *ca.* 0.5 mV h^{-1} over 100 h. The latter numbers attest to both the inferior activity and durability of this catalyst. Based on our observations in Figure 6a,b, it appears that the SV allows for regaining significant fraction of performance lost by Ni XG/KB-2:1−300 catalyst (*ca.* 110 mV) and Ni/VC catalyst (*ca.* 50 mV). While evidence for the recovery mechanism is not yet known, we can speculate that it is related to the removal of surface species blocking catalytic active sites and/or the removal of hydrogen bubbles, both facilitated by changing electrode potential during SV testing.

HAADF-STEM and STEM-EDS images for the Ni-XG/KB-2:1−300 catalyst after the durability testing are shown in Figure 7 (see HAADF-STEM and STEM-EDS images at the BOT in Figure 4a−e), whereas XPS characterization data for the Ni-XG/KB-2:1−300 catalyst before and after the durability testing are shown in Figures S11 and S12. The images in Figure 7a,b attest to some particle agglomeration during the durability test (see Figure S13 for the durability test where images in Figure 7 were taken afterward), possibly resulting in the active surface area loss. Figure 7c−f also reveals partial deformation of the oxygen-rich layer in the nanoparticle after the durability testing. The XPS survey data in Figure S11 and in Table S7 show similar elemental compositions for catalysts before and after testing: 52−56 at % C, *ca.* 11 at % O, *ca.* 4 at % Ni, 26−30 at % F, plus small quantities of N and Cl (≤1 at %). The lack of a significant change in the catalyst composition during testing is confirmed by high-resolution C 1s, O 1s, and -Ni 2p spectra in Figure S12. The C 1s spectra in Figure S12a show two large peaks *ca.* 284.6 eV and *ca.* 292 eV, assigned to C−C and to C−F_x bonds, respectively. Peak assigned to C−F_x bonds is due to the presence of Nafion in the catalyst ink.[47] Two small peaks, assigned to C−O and O═C−O bonds, are also observed.[35] Regarding the O 1s, in Figure S12b, both samples showed multiple O species: O−Ni, O that is part of hydroxide, O that is assigned to O−C bonds, and a peak at *ca.* 535 eV that is likely due to the adsorbed water.[18] The Ni 2p spectrum in Figure S12c is somewhat distorted because of the overlap with F-Auger features at *ca.* 861 and 879 eV. For the most part, the Ni 2p spectrum appears to be primarily Ni-hydroxide.[18] No significant changes were detected in the near-surface composition that could explain the activity loss in the durability test. The absence of metallic signature in both samples is likely due to the hydroxide layer growing thicker during HER testing.[31]

AEMWE Testing. AEMWE testing was performed with two HER catalysts: the Ni-XG/KB-2:1−300 catalyst heat-treated for 2 h and PtRu/C (a state-of-the-art PGM benchmark catalyst) using a PGM-free PTL-supported (ionomer-free) NiFe/Ni-foam anode catalyst in both cases. Polarization curves recorded with both catalysts at 70 °C are shown in Figure 8a. The HFR-free voltage difference between MEAs with the PGM and PGM-free cathodes, amounting to *ca.* 0.1 V at a current density of 0.1 A cm^{-2}, increases to *ca.* 0.25 V at higher current densities of 1−2 A cm^{-2} (Table S8). A fully PGM-free AEMWE operating with Ni-XG/KB-2:1−300 catalyst at the cathode reached 1.95 V at 1 A cm^{-2} which demonstrates superior performance compared to previously reported works.[48−50] The HFR value measured with the fully PGM-free MEA is by *ca.* 0.01 Ω cm^2 higher than that for the MEA with the PGM cathode, likely due to a thicker catalyst layer (Figure S14) because of the higher catalyst loading. The Nyquist plots recorded with both MEAs at a current density of 0.4 A cm^{-2} comprise two semicircles (Figure 8b). Vincent et al. attributed the semicircle at higher frequencies to the charge-transfer resistance of the anode and the one at lower frequencies to the charge-transfer resistance of the cathode,[51] which was confirmed in our experiments. We used the same PTL-supported NiFe/Ni-foam catalyst at both anodes, which resulted in high-frequency semicircles of the same diameter. Not surprisingly, this was not the case for the low-frequency semicircles in the two cases as they involved different HER catalysts. A smaller diameter was observed with the PGM cathode, attesting to faster HER kinetics at PtRu/C than that at Ni-XG/KB-2:1−300.

Durability performance of the fully PGM-free MEA was assessed at 80 °C *via* a constant-current hold at 1 A cm^{-2} for 5 h (Figure 8c). The MEA with Ni-XG/KB-2:1−300 catalyst showed a high BOT performance, with a current density of 1 A cm^{-2} reached at 1.90 V (1.84 V HFR-free), a *ca.* 50 mV improvement over the test recorded at 70 °C, Figure 8a,d. The voltage loss at 1 A cm^{-2}, calculated from the difference in voltage values at BOT and EOT (polarization curves in Figure 8d), is *ca.* 0.05 V. The corresponding performance degradation may be attributed to several factors such as the anode and/or cathode catalyst deactivation, ionic conductivity loss within the cathode catalyst layer, or membrane and ionomer degradation.[52] Identification of the dominant degradation pathway and systematic optimization of the MEA fabrication process are expected to be key to further improvements in the PGM-free AEMWE performance.

CONCLUSION

In this study, a sol−gel method was used to synthesize xerogel-derived Ni catalysts supported on carbon with synthesis conditions largely deciding HER activity of the resulting materials. Carbon support was found to be key to achieving a uniform distribution of Ni nanoparticles and preventing severe particle agglomeration that can otherwise occur during heat treatment. Physicochemical characterization revealed the

https://doi.org/10.1021/acsaem.5c01048
ACS Appl. Energy Mater. XXXX, XXX, XXX−XXX

formation of a few nanometers thick, partially oxidized layer on the outside of the nanoparticles. It is hypothesized that the hydroxide species present in this layer play an important role in facilitating dissociative adsorption of water and formation of hydrogen intermediates on adjacent Ni sites, ultimately leading to H_2 evolution.

The catalyst heat-treated at a relatively low temperature of 300 °C for 2 h showed the highest HER activity of all studied xerogel-derived catalysts, likely due to an optimal ratio of metallic Ni to $Ni(OH)_2$ at the surface. In general, the Ni-XG/KB catalysts exhibited better activity and durability than the commercial Ni/VC catalyst. The most active of these catalysts was used in the cathode of a fully PGM-free AEMWE, reaching a highly respectable performance (1.90 V at 1 A cm^{-2}).

■ ASSOCIATED CONTENT

Supporting Information

The Supporting Information is available free of charge at https://pubs.acs.org/doi/10.1021/acsaem.5c01048.

Additional catalyst characterization and electrochemical measurements (PDF)

■ AUTHOR INFORMATION

Corresponding Authors

Doha M. Sayed − *Materials Physics and Applications Division, Los Alamos National Laboratory, Los Alamos, New Mexico 87545, United States;* orcid.org/0000-0002-7313-3467; Email: doha@lanl.gov

Piotr Zelenay − *Materials Physics and Applications Division, Los Alamos National Laboratory, Los Alamos, New Mexico 87545, United States;* orcid.org/0000-0002-8962-9520; Email: zelenay@lanl.gov

Authors

Luigi Osmieri − *Materials Physics and Applications Division, Los Alamos National Laboratory, Los Alamos, New Mexico 87545, United States;* orcid.org/0000-0002-3111-2270

Haoran Yu − *Center for Nanophase Materials Sciences, Oak Ridge National Laboratory, Oak Ridge, Tennessee 37831, United States;* orcid.org/0000-0001-7304-2840

Lynda Amichi − *Center for Nanophase Materials Sciences, Oak Ridge National Laboratory, Oak Ridge, Tennessee 37831, United States*

Harry M. Meyer III − *Chemical Sciences Division, Oak Ridge National Laboratory, Oak Ridge, Tennessee 37831, United States*

Jeremy D. Jernigen − *Materials Physics and Applications Division, Los Alamos National Laboratory, Los Alamos, New Mexico 87545, United States*

Complete contact information is available at: https://pubs.acs.org/10.1021/acsaem.5c01048

Notes

The authors declare no competing financial interest.

■ ACKNOWLEDGMENTS

This work was funded by the U.S. Department of Energy (DOE), Energy Efficiency and Renewable Energy, Hydrogen and Fuel Cell Technologies Office through Electrocatalysis Consortium (ElectroCat). Funding was also provided by the Los Alamos National Laboratory Directed Research & Development (LDRD) project 20210953PRD3. The authors would like to thank Kimberly S. Reeves (Center for Nanophase Materials Sciences, Oak Ridge National Laboratory) for preparing TEM specimens. This work was authored in part by Los Alamos National Laboratory operated by Triad National Security, LLC under US DOE contract no. 89233218CNA000001 and by Oak Ridge National Laboratory operated by UT-Battelle, LLC, under contract no. DE-AC05-00OR22725. STEM research was conducted as part of a user project at the Center for Nanophase Materials Sciences (CNMS), which is a US Department of Energy, Office of Science User Facility at Oak Ridge National Laboratory. The authors acknowledge Melissa E. Kreider and Shaun M. Alia for the discussion.

■ REFERENCES

(1) Rogelj, J.; Schaeffer, M.; Meinshausen, M.; Knutti, R.; Alcamo, J.; Riahi, K.; Hare, W. Zero Emission Targets as Long-Term Global Goals for Climate Protection. *Environ. Res. Lett.* **2015**, *10* (10), 105007.

(2) van Soest, H. L.; den Elzen, M. G. J.; van Vuuren, D. P. Net-Zero Emission Targets for Major Emitting Countries Consistent with the Paris Agreement. *Nat. Commun.* **2021**, *12* (1), 2140.

(3) Oliveira, A. M.; Beswick, R. R.; Yan, Y. A Green Hydrogen Economy for a Renewable Energy Society. *Curr. Opin. Chem. Eng.* **2021**, *33*, 100701.

(4) Miller, H. A.; Bouzek, K.; Hnat, J.; Loos, S.; Bernäcker, C. I.; Weißgärber, T.; Röntzsch, L.; Meier-Haack, J. Green Hydrogen from Anion Exchange Membrane Water Electrolysis: A Review of Recent Developments in Critical Materials and Operating Conditions. *Sustain. Energy Fuels* **2020**, *4* (5), 2114−2133.

(5) Mayyas, A. T.; Ruth, M. F.; Pivovar, B. S.; Bender, G.; Wipke, K. B. *Manufacturing Cost Analysis for Proton Exchange Membrane Water Electrolyzers*; Golden, CO (United States), 2019..

(6) Alia, S.; Ding, D.; McDaniel, A.; Toma, F. M.; Dinh, H. N. Chalkboard 2 - How to Make Clean Hydrogen. *Electrochem. Soc. Interface* **2021**, *30* (4), 49−56.

(7) Mandal, M. Recent Advancement on Anion Exchange Membranes for Fuel Cell and Water Electrolysis. *ChemElectroChem.* **2021**, *8* (1), 36−45.

(8) Faid, A. Y.; Sunde, S. Anion Exchange Membrane Water Electrolysis from Catalyst Design to the Membrane Electrode Assembly. *Energy Technol.* **2022**, *10* (9), 2200506.

(9) Vij, V.; Sultan, S.; Harzandi, A. M.; Meena, A.; Tiwari, J. N.; Lee, W.-G.; Yoon, T.; Kim, K. S. Nickel-Based Electrocatalysts for Energy-Related Applications: Oxygen Reduction, Oxygen Evolution, and Hydrogen Evolution Reactions. *ACS Catal.* **2017**, *7* (10), 7196−7225.

(10) Moschkowitsch, W.; Lori, O.; Elbaz, L. Recent Progress and Viability of PGM-Free Catalysts for Hydrogen Evolution Reaction and Hydrogen Oxidation Reaction. *ACS Catal.* **2022**, *12* (2), 1082−1089.

(11) Zhu, Z.; Lin, Y.; Fang, P.; Wang, M.; Zhu, M.; Zhang, X.; Liu, J.; Hu, J.; Xu, X. Orderly Nanodendritic Nickel Substitute for Raney Nickel Catalyst Improving Alkali Water Electrolyzer. *Adv. Mater.* **2024**, *36* (1), 2307035.

(12) Feidenhans'l, A. A.; Regmi, Y. N.; Wei, C.; Xia, D.; Kibsgaard, J.; King, L. A. Precious Metal Free Hydrogen Evolution Catalyst Design and Application. *Chem. Rev.* **2024**, *124* (9), 5617−5667.

(13) Zhuang, Z.; Giles, S. A.; Zheng, J.; Jenness, G. R.; Caratzoulas, S.; Vlachos, D. G.; Yan, Y. Nickel Supported on Nitrogen-Doped Carbon Nanotubes as Hydrogen Oxidation Reaction Catalyst in Alkaline Electrolyte. *Nat. Commun.* **2016**, *7* (1), 10141.

(14) Wei, C.; Rao, R. R.; Peng, J.; Huang, B.; Stephens, I. E. L.; Risch, M.; Xu, Z. J.; Shao-Horn, Y. Recommended Practices and Benchmark Activity for Hydrogen and Oxygen Electrocatalysis in Water Splitting and Fuel Cells. *Adv. Mater.* **2019**, *31* (31), 1806296.

(15) Orozco, F.; Salvatore, A.; Sakulmankongsuk, A.; Gomes, D. R.; Pei, Y.; Araya-Hermosilla, E.; Pucci, A.; Moreno-Villoslada, I.;

Picchioni, F.; Bose, R. K. Electroactive Performance and Cost Evaluation of Carbon Nanotubes and Carbon Black as Conductive Fillers in Self-Healing Shape Memory Polymers and Other Composites. *Polymer* **2022**, *260*, 125365.
(16) Hu, C.; Lv, C.; Zeng, N.; Liu, A.; Liu, Y.; Hu, L.; Li, P.; Yao, Y.; Cai, J.; Tang, T. Recent Advances in Ni-Based Electrocatalysts for Hydrogen Evolution Reaction. *Energy Technol.* **2023**, *11* (1), 2201048.
(17) Liu, J.; Wang, Z.; Zhang, D.; Qin, Y.; Xiong, J.; Lai, J.; Wang, L. Systematic Engineering on Ni-Based Nanocatalysts Effectively Promote Hydrogen Evolution Reaction. *Small* **2022**, *18* (13), 2108072.
(18) Osmieri, L.; Yu, H.; Hermann, R. P.; Kreider, M. E.; Meyer, H. M.; Kropf, A. J.; Park, J. H.; Alia, S. M.; Cullen, D. A.; Myers, D. J.; Zelenay, P. Aerogel-Derived Nickel-Iron Oxide Catalysts for Oxygen Evolution Reaction in Alkaline Media. *Appl. Catal. B: Environ.* **2024**, *348*, 123843.
(19) Moschkowitsch, W.; Zion, N.; Honig, H. C.; Levy, N.; Cullen, D. A.; Elbaz, L. Mixed-Metal Nickel−Iron Oxide Aerogels for Oxygen Evolution Reaction. *ACS Catal.* **2022**, *12* (19), 12162−12169.
(20) Job, N.; Théry, A.; Pirard, R.; Marien, J.; Kocon, L.; Rouzaud, J.-N.; Béguin, F.; Pirard, J.-P. Carbon Aerogels, Cryogels and Xerogels: Influence of the Drying Method on the Textural Properties of Porous Carbon Materials. *Carbon* **2005**, *43* (12), 2481−2494.
(21) De, A.; Kim, M. S.; Adhikari, A.; Patel, R.; Kundu, S. Sol−Gel-Derived Nanostructured Electrocatalysts for Oxygen Evolution Reaction: A Review. *J. Mater. Chem. A* **2024**, *12* (31), 19720−19756.
(22) Wu, J.; Yang, Z.; Sun, Q.; Li, X.; Strasser, P.; Yang, R. Synthesis and Electrocatalytic Activity of Phosphorus-Doped Carbon Xerogel for Oxygen Reduction. *Electrochim. Acta* **2014**, *127*, 53−60.
(23) Chekin, F. Sol−Gel Synthesis of Palladium Nanoparticles Supported on Reduced Graphene Oxide: An Active Electrocatalyst for Hydrogen Evolution Reaction. *Bull. Mater. Sci.* **2015**, *38* (4), 887−893.
(24) Peera, S. G.; Koutavarapu, R.; Prasada Reddy, P. S.; Koyyada, G.; Alodhayb, A. N.; Pandiaraj, S.; Kim, S. W.; Tamtam, M. R. Effect of N-Doped Carbon on the Morphology and Oxygen Reduction Reaction (ORR) Activity of a Xerogel-Derived Mn(II)O Electrocatalyst. *Catalysts* **2024**, *14* (11), 792.
(25) Osmieri, L.; He, Y.; Chung, H. T.; McCool, G.; Zulevi, B.; Cullen, D. A.; Zelenay, P. La−Sr−Co Oxide Catalysts for Oxygen Evolution Reaction in Anion Exchange Membrane Water Electrolyzer: The Role of Electrode Fabrication on Performance and Durability. *J. Power Sources* **2023**, *556*, 232484.
(26) Xiao, J.; Oliveira, A. M.; Wang, L.; Zhao, Y.; Wang, T.; Wang, J.; Setzler, B. P.; Yan, Y. Water-Fed Hydroxide Exchange Membrane Electrolyzer Enabled by a Fluoride-Incorporated Nickel−Iron Oxyhydroxide Oxygen Evolution Electrode. *ACS Catal.* **2021**, *11* (1), 264−270.
(27) Babaei, E.; Bazyari, A. Effects of Drying Conditions on Physicochemical Properties of Epoxide Sol−gel Derived α-Fe_2O_3 and NiO: A Comparison between Xerogels and Aerogels. *Ceram. Int.* **2022**, *48* (22), 33340−33349.
(28) Tüysüz, H.; Schüth, F. Ordered Mesoporous Materials as Catalysts. *Adv. Catal.* **2012**, *55*, 127−239.
(29) Jiang, Z.; Liao, X.; Zhao, Y. Comparative Study of the Dry Reforming of Methane on Fluidised Aerogel and Xerogel Ni/Al_2O_3 Catalysts. *Appl. Petrochem. Res.* **2013**, *3*, 91−99.
(30) Heinius, L.; Klingenhof, M.; Weiser, G.; Schröer, P.; Metzler, L.; Koch, S.; Selve, S.; Vierrath, S.; Strasser, P. Design and Analysis of Carbon-Supported NiMo HER Catalysts and Electrodes for High Performance All PGM-Free AEM Electrolysers. *Electrochem. Sci. Adv.* **2025**, No. e2024000275.
(31) Hall, D. S.; Bock, C.; MacDougall, B. R. The Electrochemistry of Metallic Nickel: Oxides, Hydroxides, Hydrides and Alkaline Hydrogen Evolution. *J. Electrochem. Soc.* **2013**, *160* (3), F235−F243.
(32) Bae, S.-Y.; Mahmood, J.; Jeon, I.-Y.; Baek, J.-B. Recent Advances in Ruthenium-Based Electrocatalysts for the Hydrogen Evolution Reaction. *Nanoscale Horiz* **2020**, *5* (1), 43−56.
(33) Anantharaj, S.; Noda, S.; Jothi, V. R.; Yi, S.; Driess, M.; Menezes, P. W. Strategies and Perspectives to Catch the Missing Pieces in Energy-Efficient Hydrogen Evolution Reaction in Alkaline Media. *Angew. Chem., Int. Ed.* **2021**, *60* (35), 18981−19006.
(34) Kibsgaard, J.; Chorkendorff, I. Considerations for the Scaling-up of Water Splitting Catalysts. *Nat. Energy* **2019**, *4* (6), 430.
(35) Campos-Roldán, C. A.; Parnière, A.; Donzel, N.; Pailloux, F.; Blanchard, P.-Y.; Jones, D. J.; Rozière, J.; Cavaliere, S. Influence of the Carbon Support on the Properties of Platinum−Yttrium Nanoalloys for the Oxygen Reduction Reaction. *ACS Appl. Energy Mater.* **2022**, *5* (3), 3319−3328.
(36) Katić, J.; Metikoš−Huković, M.; Peter, R.; Petravić, M. The Electronic Structure of the α−$Ni(OH)_2$ Films: Influence on the Production of the High−Performance Ni−Catalyst Surface. *J. Power Sources* **2015**, *282*, 421−428.
(37) Xue, S.; Liang, Y.; Hou, S.; Zhang, Y.; Jiang, H. Alpha-Nickel Hydroxide Coating of Metallic Nickel for Enhanced Alkaline Hydrogen Evolution. *ChemSusChem* **2022**, *15* (18), No. e202201072.
(38) Wang, J.; Ge, X.; Liu, Z.; Thia, L.; Yan, Y.; Xiao, W.; Wang, X. Heterogeneous Electrocatalyst with Molecular Cobalt Ions Serving as the Center of Active Sites. *J. Am. Chem. Soc.* **2017**, *139* (5), 1878−1884.
(39) Wang, J.; Gan, L.; Zhang, W.; Peng, Y.; Yu, H.; Yan, Q.; Xia, X.; Wang, X. In Situ Formation of Molecular Ni-Fe Active Sites on Heteroatom-Doped Graphene as a Heterogeneous Electrocatalyst toward Oxygen Evolution. *Sci. Adv.* **2018**, *4* (3), No. eaap7970.
(40) Walter, C.; Menezes, P. W.; Driess, M. Perspective on Intermetallics towards Efficient Electrocatalytic Water-Splitting. *Chem. Sci.* **2021**, *12* (25), 8603−8631.
(41) Subbaraman, R.; Tripkovic, D.; Strmcnik, D.; Chang, K.-C.; Uchimura, M.; Paulikas, A. P.; Stamenkovic, V.; Markovic, N. M. Enhancing Hydrogen Evolution Activity in Water Splitting by Tailoring Li^+-Ni$(OH)_2$-Pt Interfaces. *Science* **2011**, *334* (6060), 1256−1260.
(42) Wang, B.; Sun, H.; Chen, M.; Zhou, T.; Zheng, H.; Zhang, M.; Xiao, B.; Zhao, J.; Zhang, Y.; Zhang, J.; Liu, Q. Ru Single-Atom Regulated Ni$(OH)_2$ Nanowires Coupled with FeOOH to Achieve Highly Efficient Overall Water Splitting at Industrial Current Density. *Chem. Eng. J.* **2024**, *479*, 147500.
(43) Gong, M.; Zhou, W.; Tsai, M.-C.; Zhou, J.; Guan, M.; Lin, M.-C.; Zhang, B.; Hu, Y.; Wang, D.-Y.; Yang, J.; Pennycook, S. J.; Hwang, B.-J.; Dai, H. Nanoscale Nickel Oxide/Nickel Heterostructures for Active Hydrogen Evolution Electrocatalysis. *Nat. Commun.* **2014**, *5* (1), 4695.
(44) Huang, J.; Han, J.; Wu, T.; Feng, K.; Yao, T.; Wang, X.; Liu, S.; Zhong, J.; Zhang, Z.; Zhang, Y.; Song, B. Boosting Hydrogen Transfer during Volmer Reaction at Oxides/Metal Nanocomposites for Efficient Alkaline Hydrogen Evolution. *ACS Energy Lett.* **2019**, *4* (12), 3002−3010.
(45) Kou, T.; Chen, M.; Wu, F.; Smart, T. J.; Wang, S.; Wu, Y.; Zhang, Y.; Li, S.; Lall, S.; Zhang, Z.; Liu, Y. S.; Guo, J.; Wang, G.; Ping, Y.; Li, Y. Carbon Doping Switching on the Hydrogen Adsorption Activity of NiO for Hydrogen Evolution Reaction. *Nat. Commun.* **2020**, *11* (1), 590.
(46) Yang, Y.; Sun, X.; Han, G.; Liu, X.; Zhang, X.; Sun, Y.; Zhang, M.; Cao, Z.; Sun, Y. Enhanced Electrocatalytic Hydrogen Oxidation on Ni/NiO/C Derived from a Nickel-Based Metal−Organic Framework. *Angew. Chem., Int. Ed.* **2019**, *58* (31), 10644.
(47) Volk, E. K.; Kreider, M. E.; Kwon, S.; Alia, S. M. Recent Progress in Understanding the Catalyst Layer in Anion Exchange Membrane Electrolyzers − Durability, Utilization, and Integration. *EES Catal* **2024**, *2* (1), 109−137.
(48) López-Fernández, E.; Gil-Rostra, J.; Espinós, J. P.; González-Elipe, A. R.; de Lucas Consuegra, A.; Yubero, F. Chemistry and Electrocatalytic Activity of Nanostructured Nickel Electrodes for Water Electrolysis. *ACS Catal.* **2020**, *10* (11), 6159−6170.
(49) Jiang, X.; Kyriakou, V.; Wang, B.; Deng, S.; Costil, S.; Chen, C.; Liu, T.; Deng, C.; Liao, H.; Jiang, T. Hierarchical Microporous Ni-Based Electrodes Enable "Two Birds with One Stone" in Highly

https://doi.org/10.1021/acsaem.5c01048
ACS Appl. Energy Mater. XXXX, XXX, XXX−XXX

Efficient and Robust Anion Exchange Membrane Water Electrolysis (AEMWE). *Chem. Eng. J.* **2024**, *486*, 150180.
(50) Carbone, A.; Zignani, S. C.; Gatto, I.; Trocino, S.; Aricò, A. S. Assessment of the FAA3−50 Polymer Electrolyte in Combination with a $NiMn_2O_4$ Anode Catalyst for Anion Exchange Membrane Water Electrolysis. *Int. J. Hydrogen Energy* **2020**, *45* (16), 9285−9292.
(51) Vincent, I.; Lee, E.-C.; Kim, H.-M. Comprehensive Impedance Investigation of Low-Cost Anion Exchange Membrane Electrolysis for Large-Scale Hydrogen Production. *Sci. Rep.* **2021**, *11* (1), 293.
(52) Lim, J.; Klein, J. M.; Lee, S. G.; Park, E. J.; Kang, S. Y.; Maurya, S.; Mustain, W. E.; Boettcher, S.; Kim, Y. S. Addressing the Challenge of Electrochemical Ionomer Oxidation in Future Anion Exchange Membrane Water Electrolyzers. *ACS Energy Lett.* **2024**, *9*, 3074−3083.

https://doi.org/10.1021/acsaem.5c01048
ACS Appl. Energy Mater. XXXX, XXX, XXX−XXX